Accuracy of magnetic resonance based susceptibility measurements

Hannah E. Erdevig, Stephen E. Russek, Slavka Carnicka, Karl F. Stupic, and Kathryn E. Keenan

Citation: AIP Advances **7**, 056718 (2017); doi: 10.1063/1.4975700
View online: http://dx.doi.org/10.1063/1.4975700
View Table of Contents: http://aip.scitation.org/toc/adv/7/5
Published by the American Institute of Physics

Accuracy of magnetic resonance based susceptibility measurements

Hannah E. Erdevig,[1,2] Stephen E. Russek,[1] Slavka Carnicka,[1]
Karl F. Stupic,[1] and Kathryn E. Keenan[1]
[1]*Physical Measurement Laboratory, NIST, Boulder, Colorado 80305, USA*
[2]*Department of Physics, University of Colorado Boulder, Boulder, Colorado 80309, USA*

(Presented 1 November 2016; received 23 September 2016; accepted 10 November 2016; published online 6 February 2017)

Magnetic Resonance Imaging (MRI) is increasingly used to map the magnetic susceptibility of tissue to identify cerebral microbleeds associated with traumatic brain injury and pathological iron deposits associated with neurodegenerative diseases such as Parkinson's and Alzheimer's disease. Accurate measurements of susceptibility are important for determining oxygen and iron content in blood vessels and brain tissue for use in noninvasive clinical diagnosis and treatment assessments. Induced magnetic fields with amplitude on the order of 100 nT, can be detected using MRI phase images. The induced field distributions can then be inverted to obtain quantitative susceptibility maps. The focus of this research was to determine the accuracy of MRI-based susceptibility measurements using simple phantom geometries and to compare the susceptibility measurements with magnetometry measurements where SI-traceable standards are available. The susceptibilities of paramagnetic salt solutions in cylindrical containers were measured as a function of orientation relative to the static MRI field. The observed induced fields as a function of orientation of the cylinder were in good agreement with simple models. The MRI susceptibility measurements were compared with SQUID magnetometry using NIST-traceable standards. MRI can accurately measure relative magnetic susceptibilities while SQUID magnetometry measures absolute magnetic susceptibility. Given the accuracy of moment measurements of tissue mimicking samples, and the need to look at small differences in tissue properties, the use of existing NIST standard reference materials to calibrate MRI reference structures is problematic and better reference materials are required. [http://dx.doi.org/10.1063/1.4975700]

INTRODUCTION

Quantitative Susceptibility Mapping (QSM)[1] using Magnetic Resonance Imaging (MRI) is increasingly used instead of qualitative techniques, such as susceptibility weighted imaging,[2] to map neurological conditions,[3–5] blood oxygen content,[6] and iron overload in the heart and liver.[7] Some neurodegenerative diseases, such as Parkinson's and Alzheimer's disease, have been associated with excess iron in the brain.[8,9] A reproducible and quantitative method to measure blood-oxygen content via QSM is particularly important for finding and determining the severity of cerebral microbleeds resulting from stroke or traumatic brain injury.[10] QSM may be important for measuring iron overload in the heart and liver, caused by diseases such as hemochromatosis, because iron can catalyze the conversion of hydrogen peroxide into free radicals, causing damage to cell membranes, proteins, and DNA.[11] Tissue property measurements using QSM are also advantageous compared to SQUID (superconducting quantum interference device) magnetometry measurements since the latter are done on excised tissue and are inaccurate due to water loss, blood oxidation, and volume changes. However, there is much left to do to validate the accuracy of QSM and of MRI-based susceptibility

measurements in general. Accurate in-vivo measurements of magnetic susceptibility, along with the necessary calibrations and post-processing techniques, are required to use magnetic susceptibility as a quantitative biomarker. Creating standard measurement protocols and a phantom with NIST verified susceptibility samples would help ensure site-to-site comparability of data and allow QSM to be more widely and reliably used in clinical applications. In-vivo MRI susceptibility measurements, if done properly, may become the gold standard for tissue susceptibility quantification. The first step is to verify the accuracy of MRI susceptibility measurements relative to other traditional methods.

TISSUE SUSCEPTIBILITY AND TISSUE MIMICS

Tissue is predominantly diamagnetic at body temperature 310 K and room temperature 300 K. This is seen in Fig. 1a, which shows the magnetic moment vs. field for cow liver. The magnetic susceptibility is dominated by the diamagnetic susceptibilities of water (-9.05 x 10^{-6}) and fat (typically -10.0 x 10^{-6}).[12] All susceptibility values in this paper are reported in SI units. The complex magnetic structure of tissue is seen at lower temperatures. Fig. 1a shows a decrease in the diamagnetic (negative) slope as the temperature decreases indicating the presence of a paramagnetic component. At low temperature (1.8 K) there is a deviation in linearity due to paramagnetic and ferrimagnetic components. The presence of a ferrimagnetic component is seen in Fig. 1b, which plots the moment vs. inverse temperature. If there were only a paramagnetic component, the data would be linear. For liver, the paramagnetic and ferrimagnetic components are predominantly due to blood iron in deoxygenated hemoglobin and iron oxide deposits (ferritin).

To mimic the susceptibility properties of tissue, one can use a solution of paramagnetic salts in water. Fig. 1d demonstrates how the diamagnetic susceptibility of water, with minimal temperature-dependence, and a paramagnetic component can roughly approximate the magnetic properties of tissue. We present data from $GdCl_3$ solutions, whose magnetic properties are shown in Fig. 1c,d

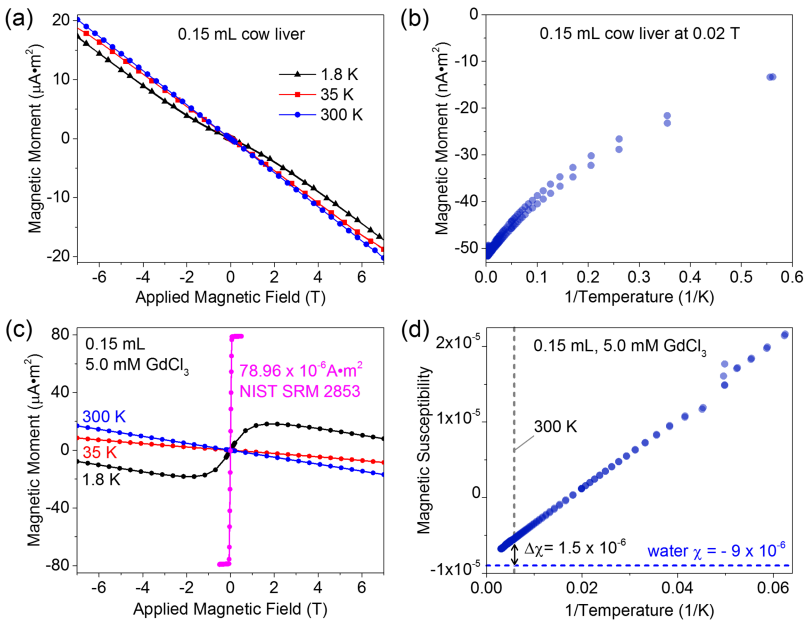

FIG. 1. (a) SQUID magnetometer measurements of magnetic moment vs. applied field for a sample of cow liver. (b) Magnetic moment vs. inverse temperature, upon heating and cooling, of the same sample. (c) SQUID magnetometer measurements of the magnetic moment vs. applied field of the 5.0 mM $GdCl_3$ solution. Also shown is the calibration curve obtained from a NIST moment standard reference material. (d) Magnetic susceptibility vs. inverse temperature for the same solution showing paramagnetic behavior. The horizontal dotted line schematically shows the diamagnetic susceptibility of water. The arrow indicates the susceptibility contribution from the Gd^{3+} ions at 300 K. Comparing the tissue magnetic properties, shown in (a) and (b), to those of the standard Gd solutions, shown in (c) and (d), one can see that the reference solutions are a good starting point to mimic the magnetic properties of tissue, although they lack the full complexity of tissue.

for a 5.0 mM solution in deionized water. The SQUID magnetometer is calibrated with a NIST YIG (yttrium iron garnet) sphere standard reference material (SRM #2852) whose room temperature moment is (79.9 ± 0.3) x 10^{-6} A·m^2. The moment (m) vs. applied field (B_a) data can be fit assuming a paramagnetic component and a diamagnetic component:

$$m = N_{Gd} V g \mu_B J \cdot B_J \left(\frac{g J \mu_B B_a}{k_B T} \right) - \frac{\chi_w V B_a}{\mu_0} \tag{1}$$

N_{Gd} is the concentration of Gd^{3+} ions, V is the volume of the sample, g is the Landé g-factor (which is 2.0 for Gd since the angular momentum vanishes), μ_B is the Bohr magneton, J is the ion angular momentum quantum number, B_J is the Brillouin function, k_B is Boltzmann's constant, T is the temperature of the sample, χ_w is the magnitude of the diamagnetic susceptibility of water, and μ_0 is the permeability of free space. The susceptibility due to the Gd^{3+} ions can be calculated from the model (Eq. 1) using the best fit parameters and the measured volume. The measured Gd susceptibility for a 5.0 mM solution at 300 K, shown in Fig. 1d is χ_{Gd} = (1.58 ± 0.16) x 10^{-6}, comparable to the theoretical value of χ_{th} = 1.89 x 10^{-6}. The errors in the measured value come from errors in the moment measurement, the volume measurement and from the extraction of the smaller Gd moment from the larger diamagnetic moment of water. For comparison, the difference in susceptibility between deoxygenated and oxygenated blood, as measured by MRI, is (3.43 ± 0.08) x 10^{-6}.[13]

MRI SUSCEPTIBILITY MEASUREMENTS

MRI susceptibility measurements are typically done by acquiring magnitude and phase data from a gradient echo sequence with multiple echo times. Magnitude and phase images of a phantom are shown in Fig. 2a. The phase image clearly shows distortion of the phase fronts due to the enhanced susceptibility of the paramagnetic salt solution contained within the vial. The imaging was done in a 30 cm bore preclinical scanner designed to image at 1.5 T, 3.0 T, or 7.0 T. The data in this paper were obtained with a static field of B_0 = (1.502102 ± 0.000006) T. The error in the field represents the typical field variation over the active volume with a standard shimming procedure. The phase must be unwrapped and the low-spatial frequency background phase variations subtracted (Fig. 2a). Background phase variations are due to an imperfect shimming of the magnet and to susceptibility discontinuities far from the region of interest.

The difference in proton phase (inside relative to outside the vial), $\delta\phi$, after an echo time, TE, is proportional to the local induced field, δB_L, along the main field direction: $\delta\phi = \gamma_p \cdot \delta B_L \cdot$TE, where γ_p is the shielded proton gyromagnetic ratio. The local field differs from the macroscopic field and is given by the macroscopic field minus the Lorentz field. The Lorentz field is a correction to the

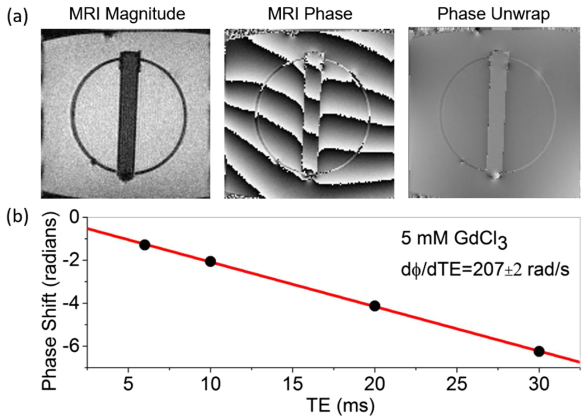

FIG. 2. (a) Magnitude and phase images of a vial containing 5.0 mM $GdCl_3$. The dark circle in the MRI amplitude image is a 76 mm diameter polycarbonate support for the vials. The third image shows the phase after unwrapping and after the long wavelength background has been subtracted. (b) Phase difference as a function of echo time (TE) taken from phase maps.

macroscopic continuum model and attempts to account for the local microscopic distribution of moments. The slope of the measured phase difference vs. echo time, as shown in Fig. 2b, will yield δB_L. The magnetic field distortion is a convolution of the magnetic susceptibility distribution, $\chi(r)$, with the magnetic dipole kernel, d(r): $\delta B_L(\vec{r}) = d(\vec{r}) \otimes \chi(\vec{r})$.[14] The susceptibility map can be obtained by inverting the field profile, although complex methods are required since this inversion is not unique.[15–18] Here, we limit our measurements to simple cylindrical geometries where the induced field is simply related to the susceptibility. For a long cylinder the internal and external field distortion is given by[19]

$$\text{Internal}: \quad \delta B_L = \frac{\Delta\chi B_0}{6}(3\cos^2\theta - 1) \tag{2a}$$

$$\text{External}: \quad \delta B_L = \frac{\Delta\chi B_0}{2} a^2/r^2 \sin^2\theta cos2\phi \tag{2b}$$

where $\Delta\chi$ is the susceptibility difference between the inside and outside of the cylinder, θ is the angle of the cylinder axis with respect to the main field, ϕ is the azimuthal angle of the observation point relative to the plane of the main field and cylinder axis, and a is the radius of the cylinder. For the simple case where the cylinder is aligned with the main field ($\theta = 0$), the susceptibility difference is given by $\Delta\chi = \frac{3\delta\phi}{\gamma_p B_0 TE}$. By measuring the slope of $\delta\phi$ vs. TE, as seen in Fig. 2b, the susceptibility can be determined. The susceptibility difference of the 5.0 mM $GdCl_3$ solution at 300 K, was (1.71 ± 0.02) x 10^{-6}, which, within error bars, agrees with the SQUID magnetometer measurements. The intrinsic errors for the SQUID measurements are larger than the MRI measurements, although the systematic errors for the MRI measurements have not yet been determined.

ANGLE DEPENDENT MEASUREMENTS

To test the orientational dependence, MRI phase maps were obtained from a phantom with vials (80 mm long, 5.0 mL volume) oriented along and perpendicular to the B_0 field. The vials were filled with 5.0 mM $GdCl_3$; the main compartment of the phantom was filled with deionized water. Line scans through the cylinders are shown in Fig. 3a along with the predicted phase change and induced fields obtained from Eq. 2a,b. Good agreement is observed, although there is some deviation at the edges of the vials, in part due to the loss of signal from the plastic vial.

To more precisely verify the orientation dependence, a rotating phantom was constructed in which the 80 mm vials could be continuously rotated while in the MRI scanner. A schematic of the rotating phantom is shown in the inset in Fig. 3b. Four 80 mm vials filled with 1.0 mM and 5.0 mM $GdCl_3$ solutions were placed in the scanner. A rod extended from the outside of the scanner to the internal rotation gears; each revolution corresponded to 19° mechanical rotation of the phantom

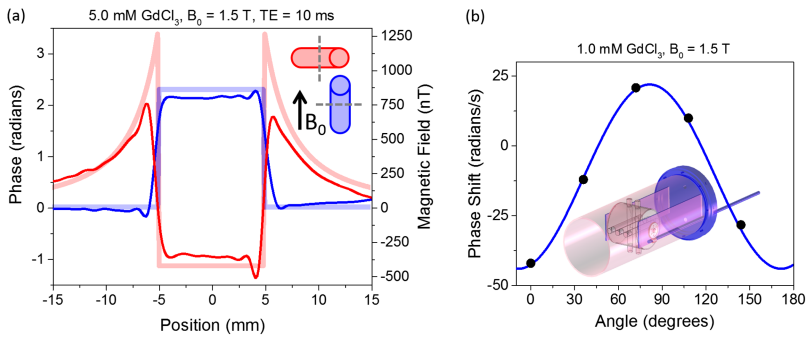

FIG. 3. (a) Line scans (opaque lines) of phase and corresponding field distortions taken with the field parallel (blue) and perpendicular (red) to the cylinder axis. When the field was perpendicular to the cylinder axis, the line scan was taken along B_0 (ϕ = 0). Also shown are the predicted phase shifts (lighter lines) from Eq. 2. (b) Plot of the change of phase with echo time within a cylinder of 1.0 mM $GdCl_3$ as a function of angle of the cylinder axis relative to the B_0 field. Also plotted is a fit using Eq. 2a (blue line). The inset a schematic of the rotating phantom used for the experiment.

insert. The change of phase between the center of each vial and the surrounding water was collected as a function of angle (Fig. 3b). The data were fit using Eq. 2a, yielding $\Delta\chi = (0.324 \pm 0.005)$ x 10^{-6} for the 1.0 mM solution.

BEYOND THE SIMPLE MODELS

A multiphysics finite element simulation with a package for modeling magnetic fields without currents was used to compute the macroscopic field of the five perpendicular vials, shown in the inset of Fig. 3b. The vials were filled with a solution with a magnetic susceptibility of 3.0 x 10^{-6} relative to the surrounding water. The numerical accuracy of the field distortion was estimated to be ±7% by varying degrees of freedom from 2 to 5 million. Finite element calculations of extremely small field perturbations on a very large B_0 field gave significant numerical errors. Fig. 4a,b show the field distortions when the B_0 field is parallel and perpendicular to the vial axes, respectively. The field profiles within the vials are not constant, as predicted by the simple models, due to the fields from neighboring vials, the finite length of the vials, and the phantom structure. Determining the local susceptibility from the full inversion of the 3-dimensional phase map should account for these distortions.

One of the main approximations in MRI-based susceptibility measurements is to assume that the local field is given by the macroscopic field, B_m, minus the Lorentz field: $B_L = B_m - \frac{2}{3}\chi B_0$. This assumes that the local microscopic fields average to zero. To determine the local field, precise microscopic calculations are needed. As a simple test, we performed a Monte Carlo simulation where 2.5 x 10^6 Gd spins were randomly distributed in 2 μm diameter sphere and 300 water molecules were allowed to diffuse throughout the volume. The fields sensed by the water molecules after a time of 0.15 ms are plotted in Fig. 4c. The Gd density corresponds to 1.0 mM concentration and an MRI-measured susceptibility of 0.32 x 10^{-6}. The microscopic field calculated from the simulation is 13.5 nT, which is much smaller than the Lorentz field B_L = 320 nT. The simulation supports the assumption that the microscopic fields due to neighboring spins average to zero, and the local field approximation is valid. For tissues, which may have more complex local geometry, this local field assumption may not be valid.

The Monte Carlo simulation gave a Gaussian distribution in microscopic fields, which had a standard deviation of 249 nT. This field distribution gives rise to a short total dephasing time T2*. The T2* value can be measured with the same data set as the susceptibility using the magnitude images and extracting the exponential decrease in the magnitude signal with echo time TE. The T2* value can be used to obtain measurements of the local iron concentration in tissue.[8] While the

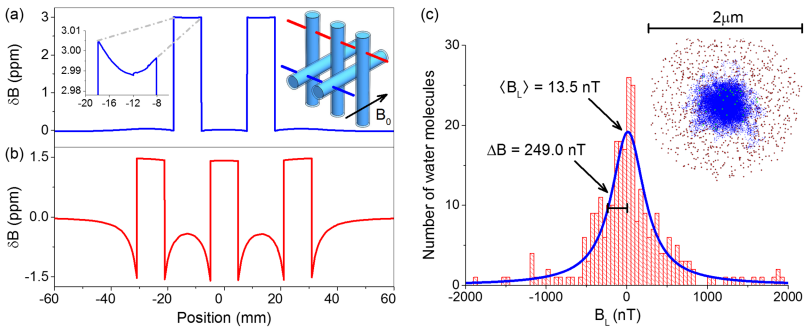

FIG. 4. Numerical calculations of the field distortions produced by the phantom shown in the inset in Fig. 3b, with five vials of paramagnetic salt solution with a susceptibility of 3.0 x 10^{-6}. The macroscopic field distribution is plotted, not the local field, since the macroscopic field is what is calculated using the macroscopic Maxwell equations. (a) The field distortion calculated by a finite element method when the vial axis is parallel to B_0 field. The inset graph shows the variation within the vial due to neighboring vials and structures. (b) The field distortion when the B_0 field is perpendicular to the axis of the vial and the line scan is taken perpendicular to both B_0 field and the vial axis. (c) Monte Carlo simulation generated histogram of microscopic fields experienced by an ensemble of water molecules diffusing (with a diffusion constant of 2.0 x 10^{-3} mm^2/s) in a 1.0 mM Gd solution. The geometry is shown in the inset with the red and blue dots representing Gd^{3+} ions and water, respectively.

decrease in T2* and the change in phase both arise, in the system studied here, from the Gd spins, T2* is strongly affected by the local microscopic structure while the phase shift is not.

CONCLUSIONS

The relative phase shifts and local induced magnetic fields can be measured very precisely with MRI. The relative susceptibilities can be accurately determined from these field shifts for simple geometries and agree with primary measurements of susceptibility where standards exist. More suitable primary standards, however, will be required to validate MRI susceptibility measurements in complex geometries. More extensive investigation into how the local field depends on microscopic tissue geometry is required to determine the accuracy of local field models.

[1] Y. Wang and T. Liu, Magn Reson Med **73**(1), 82–101 (2015).
[2] E. M. Haacke, S. Mittal, Z. Wu, J. Neelavalli, and Y. C. Cheng, AJNR Am J Neuroradiol **30**(1), 19–30 (2009).
[3] J. H. Jensen, K. Szulc, C. Hu, A. Ramani, H. Lu, L. Xuan, M. F. Falangola, R. Chandra, E. A. Knopp, J. Schenck, E. A. Zimmerman, and J. A. Helpern, Magn Reson Med **61**(2), 481–485 (2009).
[4] K. Shmueli, J. A. de Zwart, P. van Gelderen, T. Q. Li, S. J. Dodd, and J. H. Duyn, Magn Reson Med **62**(6), 1510–1522 (2009).
[5] H. Tan, T. Liu, Y. Wu, J. Thacker, R. Shenkar, A. G. Mikati, C. Shi, C. Dykstra, Y. Wang, P. V. Prasad, R. R. Edelman, and I. A. Awad, Invest Radiol **49**(7), 498–504 (2014).
[6] E. M. Haacke, K. Prabhakaran, I. R. Elangovan, Z. Wu, and J. Neelavalli, in *Susceptibility Weighted Imaging in MRI* (John Wiley & Sons, Inc., 2011), pp. 517–528.
[7] S. D. Sharma, D. Hernando, D. E. Horng, and S. B. Reeder, Magnetic Resonance in Medicine **74**(3), 673–683 (2015).
[8] F. Mitsumori, H. Watanabe, and N. Takaya, Magn Reson Med **62**(5), 1326–1330 (2009).
[9] S. Oshiro, M. S. Morioka, and M. Kikuchi, Adv Pharmacol Sci **2011**, 378278 (2011).
[10] T. Liu, K. Surapaneni, M. Lou, L. Cheng, P. Spincemaille, and Y. Wang, Radiology **262**(1), 269–278 (2012).
[11] N. C. Andrews, New England Journal of Medicine **341**(26), 1986–1995 (1999).
[12] J. F. Schenck, Medical Physics **23**(6), 815–850 (1996).
[13] V. Jain, O. Abdulmalik, K. J. Propert, and F. W. Wehrli, Magn Reson Med **68**(3), 863–867 (2012).
[14] F. Schweser, A. Deistung, B. W. Lehr, and J. R. Reichenbach, Med Phys **37**(10), 5165–5178 (2010).
[15] T. Liu, J. Liu, L. de Rochefort, P. Spincemaille, I. Khalidov, J. R. Ledoux, and Y. Wang, Magn Reson Med **66**(3), 777–783 (2011).
[16] L. de Rochefort, R. Brown, M. R. Prince, and Y. Wang, Magn Reson Med **60**(4), 1003–1009 (2008).
[17] T. Liu, P. Spincemaille, L. de Rochefort, B. Kressler, and Y. Wang, Magn Reson Med **61**(1), 196–204 (2009).
[18] Y. C. Cheng, J. Neelavalli, and E. M. Haacke, Phys Med Biol **54**(5), 1169–1189 (2009).
[19] J. Neelavalli and Y.-C. N. Cheng, in *Susceptibility Weighted Imaging in MRI* (John Wiley & Sons, Inc., 2011), pp. 17–31.